

## Neighboring V atom as a catalytic switch: Reversing the active site for exceptional water splitting

Xianbin Meng<sup>a</sup>, Zhiqiang Zhao<sup>a</sup>, Kai Li<sup>a</sup>, Youwen Liu<sup>b</sup>, Wenming Sun<sup>a\*</sup>, Tianyou Zhai<sup>b,\*</sup>, Yuqing Lin<sup>a,\*</sup>

<sup>a</sup> Department of Chemistry, Capital Normal University, Beijing 100048, PR China

<sup>b</sup> State Key Laboratory of Materials Processing and Die & Mould Technology, and School of Materials Science and Engineering, Huazhong University of Science and Technology, Wuhan 430074, PR China



### ARTICLE INFO

#### Keywords:

Water Splitting  
Reverse  
Enhancement  
Neighboring Atom  
Bifunctional Catalysts  
Electrocatalysts

### ABSTRACT

Due to the different reaction substrates involved in hydrogen evolution reaction (HER) and oxygen evolution reaction (OER), bifunctional catalysts with diverse active sites are crucial for electrochemical water splitting. However, it is extremely difficult to design sites that are catalytically active for both H- and O-containing intermediates. Herein, neighboring V site on poor-active FeN<sub>4</sub> site can reverse the active center of HER from Fe sites to N sites and simultaneously boost the activity of Fe sites for OER. Water splitting on FeV-NC requires only 1.57 V to achieve 10 mA cm<sup>-2</sup> along with an overpotential of 233.2 mV for OER and 88.8 mV for HER. Theoretical calculations reveal that the presence of neighboring V site shifts the p<sub>z</sub> centres of the bridging N atoms positively and intensifies the electronic spin and 3d orbital of Fe atoms, which optimizes the interaction of the H/O-containing reactant/intermediate on N and Fe sites.

### 1. Introduction

Electrochemical overall water splitting (OWS), one of the most promising solutions for storing intermittent solar and wind energy in the form of chemical fuels, involves two half-reactions: the hydrogen evolution reaction (HER) and the oxygen evolution reaction (OER) [1–4]. Therefore, it is crucial to develop bifunctional HER and OER electrocatalysts that can boost water electrolysis efficiency and reduce energy consumption [5–9]. However, it is extremely difficult to design sites that are catalytically active for both H- and O-containing intermediates at the same time due to the distinctly different catalytic mechanisms. Thus, active HER catalysts are often found to be poor OER catalysts, and vice versa. As the most promising alternative to noble metals, Fe-based electrocatalysts have been generally perceived for their superb catalytic properties. Excellent OER/ORR catalytic activity of FeN<sub>4</sub> site in Fe-SACs (Single-atom catalysts) has been reported [10–16], but the FeN<sub>4</sub> site has essentially negligible HER catalytic activity and consequently unsuitable as catalysts for electrocatalytic OWS. The essence of the electrocatalytic activity is the interaction between the active site with the reaction substrate/intermediate, which is closely related to the chemical state of the active center atom. Ligand identity, coordination

number and configuration of the SACs determines the performance of SACs since they directly affect the electronic state, degree of freedom and other physicochemical properties of the active center related to reactant/intermediate adsorption [17,18]. For example, replacing the non-metallic ligand N atoms in FeN<sub>4</sub> with atoms such as O, B, S, or P can modify the activity of the Fe atoms [19–22]. Nevertheless, there are few reports related to the reverse of the active site from Fe to non-metallic ligand atoms. As a transition metal adjacent to iron, vanadium also has outstanding catalytic properties, especially in the field of OWS [8, 23]. By loading a single V atom onto a C<sub>60</sub> substrate as an electrolytic water catalyst, Janssen's group illustrated the impact of electron spin states and atomic orbitals on electrocatalytic water decomposition performance [23]. Dai et al. found V SACs and DASCs have optimal HER Gibbs free energy due to the d-band centers of transition metals interact and modulate each other [8]. Therefore, the introduction of the transition metal V element into the FeN<sub>4</sub> site is expected to take advantage of the strong d-band center interactions between the two metals to modulate the HER activities of Fe and nonmetallic ligand atoms.

Herein, the active center of the HER has been reversed from Fe site to N site by introducing V atom into the FeN<sub>4</sub> site (denoted as FeV-NC), remarkably achieving exceptional water splitting catalytic activity.

\* Corresponding authors.

E-mail addresses: [swm@mail.sdu.edu.cn](mailto:swm@mail.sdu.edu.cn) (W. Sun), [zhaity@hust.edu.cn](mailto:zhaity@hust.edu.cn) (T. Zhai), [linyuqing@cnu.edu.cn](mailto:linyuqing@cnu.edu.cn) (Y. Lin).

The bimetallic FeV-NC diatomic catalysts exhibit noticeably activated electrocatalytic performance for both HER and OER, significantly outperforming single-atom catalysts (Fe-NC and V-NC). The FeV-NC/NF||FeV-NC/NF electrolyzer only needs 1.567 V to drive a current density of  $10 \text{ mA cm}^{-2}$  in 1 M KOH. In addition, under a current density of  $10 \text{ mA cm}^{-2}$ , the FeV-NC/NF||FeV-NC/NF electrolyzer still had 94 % of the current rate after 90 h of a long-term stability test. Advanced in-situ techniques and density functional theory (DFT) calculations revealed that the introduction of the V site simultaneously optimized the electronic states of the nonmetallic N and metallic Fe sites by (i) shifting the p-band center of the bridging N atom toward the Fermi energy level transfers the active activity of the HER from Fe to N and (ii) enhances the electron spin of the Fe atom while increasing the intensity of the d orbitals near the Fermi energy level, which boosts the OER activity of the Fe site (Fig. 1). These findings demonstrate the reverse of the active site between two different elements and provide a universal framework for the design and modulation of catalysts with efficiently active sites.

## 2. Experimental section

### 2.1. Synthesis of NC and Fe-NC

Typically, 1.059 g  $\text{Zn}(\text{NO}_3)_2 \cdot 6\text{H}_2\text{O}$  was dissolved in 50 mL of methanol, and then 1.23 g 2-MeIM in 50 mL of methanol was subsequently injected into the abovementioned solution under vigorous stirring for 12 h at room temperature. The as-obtained precipitates were centrifuged and washed with methanol for several times and then dried in a vacuum oven at 60 °C for another 12 h. The resulting white powder was heated in the tubular furnace to 900 °C for 1 h with Ar saturation.

In a normal procedure, 1.13 g  $\text{Zn}(\text{NO}_3)_2 \cdot 6\text{H}_2\text{O}$  and moderate  $\text{Fe}(\text{NO}_3)_3 \cdot 9\text{H}_2\text{O}$  were dissolved in 100 mL of methanol, and then 1.313 g 2-MeIM in 100 mL of methanol was subsequently injected into the abovementioned solution standing at 60 °C for 12 h, and then vigorously stirred for another 12 h at the same temperature. The as-obtained precipitates were centrifuged and washed with methanol for several times and then dried in a vacuum oven at 60 °C for 12 h, harvesting Fe-doped ZIF-8. This light yellow powder was heated in a tubular furnace to 900 °C for 1 h with Ar saturation.

## 2.2. Synthesis of FeV-NC and V-NC

In a normal procedure, 100 mg of the abovementioned Fe-doped ZIF-8 was dispersed in ethylene glycol and sonicated for 1 h at room temperature, thus forming a homogeneous suspension. A certain amount of  $\text{V}(\text{acac})_2$  (25 mg  $\text{mL}^{-1}$  in anhydrous methanol) was then added dropwise to the above suspension and sonicated for another 30 min at room temperature. The mixture was stirred for 1 h, further centrifuged and washed with anhydrous methanol for several times; The obtained precursors were dried in a vacuum oven at 60 °C overnight. Finally, the precursors were heated in the tubular furnace to 900 °C for 1 h with Ar saturation, thus obtaining FeV-NC. The V-NC was prepared in the same way as above, where Fe-doped ZIF-8 was replaced with ZIF-8.

## 3. Results and discussion

### 3.1. Morphology and structure characterization

Diatomical catalysts were prepared by using a bimetallic organic framework encapsulation strategy. As shown in Fig. 2a, the bimetallic imidazole molecular sieve framework (Fe-ZIF-8) was first synthesized by the competitive coordination of two metal ions ( $\text{Fe}^{3+}$  and  $\text{Zn}^{2+}$ ), and the vanadium acetylacetone molecule (approximately 9.9 Å) was confined into Fe-ZIF-8 (pore size 11.6 Å) by ultrasonication [10]. Subsequently, Fe-ZIF-8 encapsulated with V (denoted FeV-ZIF-8) was pyrolyzed under Ar atmosphere to obtain the final FeV-NC diatomic catalyst. Fe-NC and V-NC and metal-free NC catalysts were similarly synthesized except for being free of V, Fe and Fe/V salt.

In this synthesis process, the molar amount of  $\text{Zn}^{2+}$  is 38 times higher than that of  $\text{Fe}^{3+}$ . During the formation of Fe-ZIF-8,  $\text{Zn}^{2+}$  and  $\text{Fe}^{3+}$  form the skeleton structure of Fe-ZIF-8 by competing for coordination with the N atom of 2-MeIM. The high  $\text{Zn}^{2+}$ :  $\text{Fe}^{3+}$  molar ratio and the competitive coordination synthesis method ensured that only a small number of iron atoms were present in the skeleton and all iron atoms existed as individual atoms, which helped to inhibit the formation of iron clusters or nanoparticles from overly densely packed iron atoms during pyrolysis [10]. The evenly dispersed pore size of imidazole molecules can control the vanadium acetopyruvate in a narrow domain and prevent the aggregation of V. Moreover, Zn can form pores and defects through sublimation during high-temperature pyrolysis.

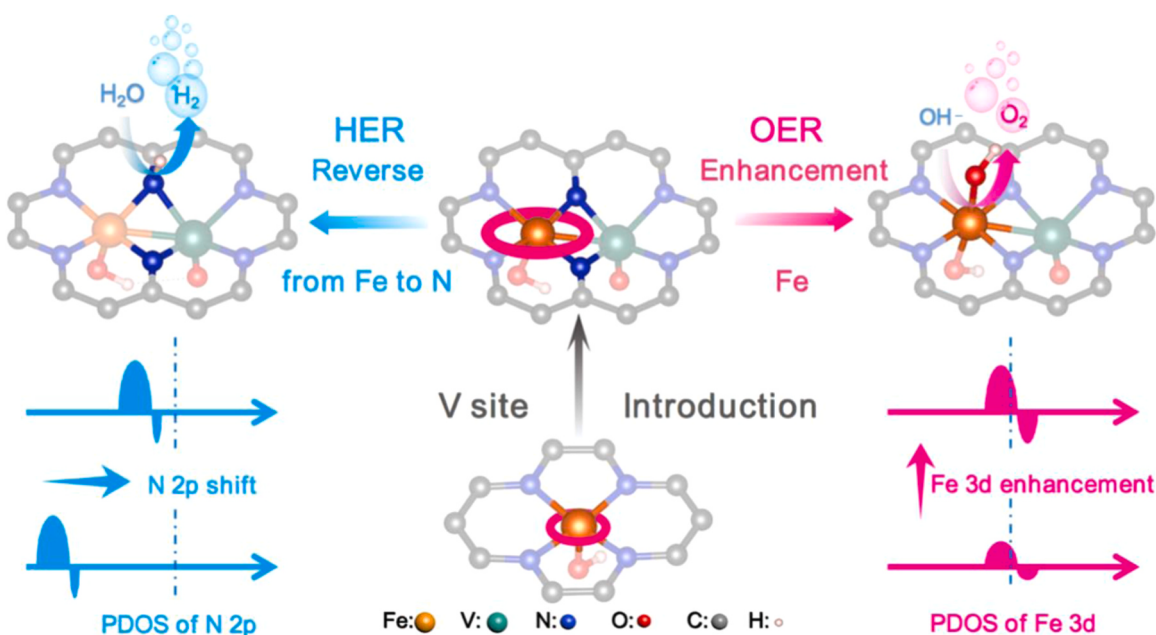


**Fig. 1.** Schematic diagram of the principle of reverse/enhancement of activation on the Fe/N sites via neighboring V atom for water splitting.

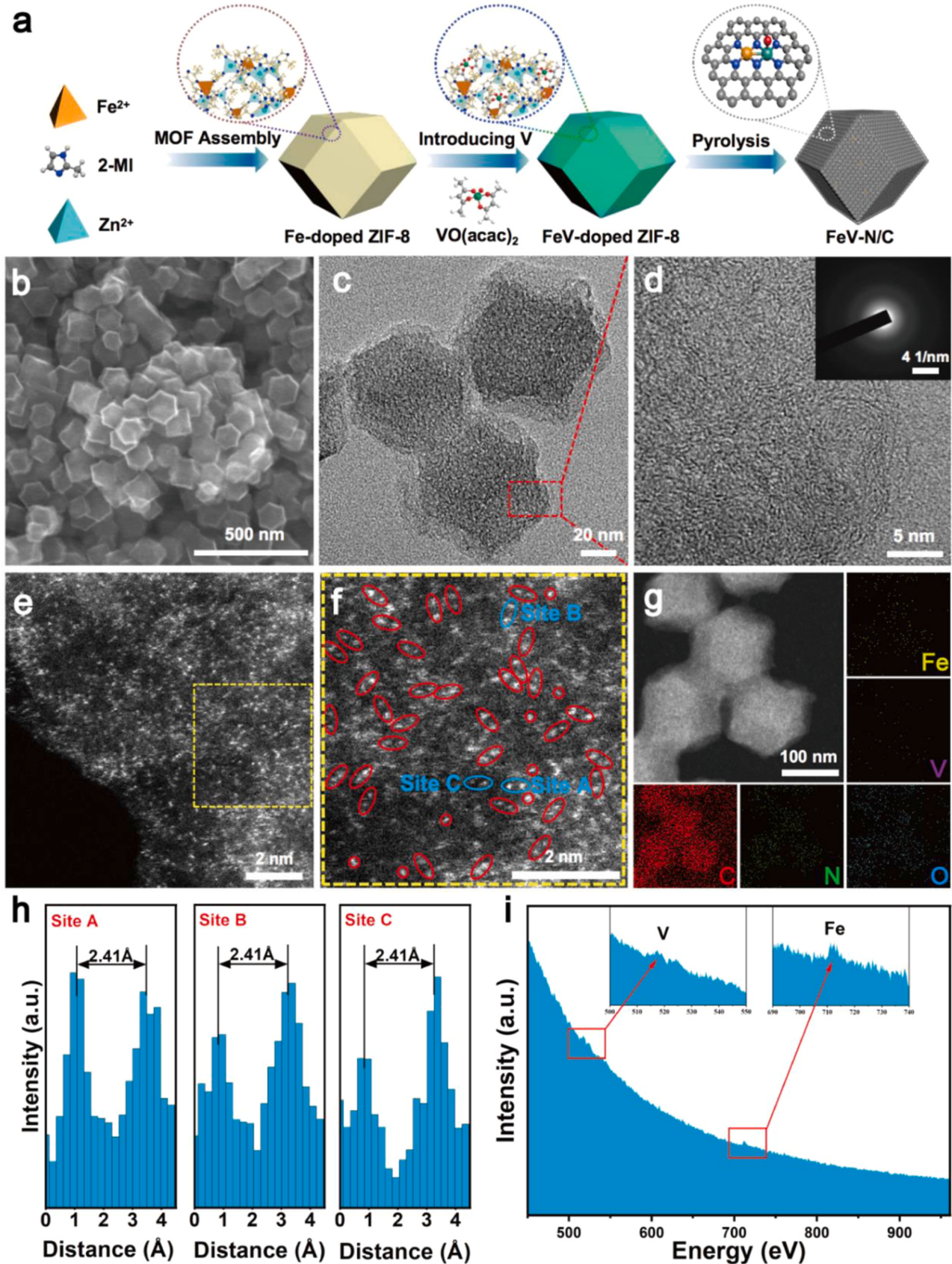


**Fig. 2.** Synthetic procedure and structural characterizations of FeV-NC. (a) Schematic illustration of the synthesis procedure for the FeV-NC. (b) SEM and (c) TEM images of FeV-NC. (d) HRTEM image and SAED image (inset) of FeV-NC. (e) Atomic resolution HAADF-STEM image and enlarged images (f) of FeV-NC. In (f), some Fe-V atomic pairs are highlighted by ellipses, and some single Fe or V atoms are highlighted by smaller circles. (g) HAADF-STEM image and EDS mappings of the corresponding C, N, O, Fe and V. (h) The intensity profiles obtained on two bimetallic FeV sites in (f). (i) EELS spectra of FeV-NC.

Mesoporous and defects are beneficial to the accessibility of active sites and the rapid transport of OWS-relevant species during electrocatalysis [12]. Raman spectroscopy (Fig. S1) shows a high intensity ratio ( $I_D/I_G$ ) of the disordered carbon-induced peak (D) relative to the graphitic carbon peak (G), also indicating the generation of structural defects on N-doped carbon supports. In addition, the difference in  $I_D/I_G$  values between the FeV-NC, Fe-NC, V-NC and NC was small, reflecting that the introduction of metal species did not affect the degree of graphitization of the NC skeleton.

Transmission electron microscopy (TEM) confirmed the successful synthesis of FeV-ZIF-8, Fe-ZIF-8, V-ZIF-8 and ZIF-8 precursor nanoparticles with uniform size and dodecahedral shape (Fig. S2). In addition, the resulting FeV-NC, Fe-NC, V-NC and NC actually inherited the dodecahedral appearance of their precursors, except that their surfaces became rough and porous (Fig. S2 and S3) [13]. Scanning electron microscopy (SEM) and TEM showed a good dodecahedron of FeV-NC during high temperature pyrolysis (Fig. 2b and c). It should be noted that there are no metal nanoparticles visible in the entire region of the HAADF-STEM image and no diffraction spots or rings in the SAED image (Fig. 2d). Aberration-corrected HAADF-STEM (Fig. 2e) further elucidated the atomically dispersed states of Fe and V, and the corresponding bright spots of the dispersed metal atoms could be clearly seen. Further magnified observation (Fig. 2f) can confirm that most Fe or V atoms appear in pairs on the N-C surface (marked by ellipses), while others appear individually (marked by circles). The coexistence of these two types of sites may be due to the excessive amount of Fe relative to V. The results of inductively coupled plasma optical emission spectroscopy (ICP-OES) showed that the Fe content in FeV-NC was 1.24 wt %, and the V content was 0.31 wt % (Table S1), thus part of the Fe may not be paired. HAADF-STEM image and corresponding elemental mappings revealed the homogeneous distribution of Fe, V, C, N, and O elements (Fig. 2g). By measuring the spacing of multiple pairs of atoms (marked with blue ellipses), the atomic Fe-V pairs are 2.41 Å apart (Fig. 2h), which lays the foundation for further DFT modeling. More importantly, the Fe-V pairs can be further identified and mapped by electron energy loss spectroscopy (EELS), as shown in Fig. 2i and Fig. S4. The Fe-L<sub>2,3</sub> edge (710.0 eV) and V-L<sub>2,3</sub> edge (517.2 eV) were simultaneously detected on an atomic pair, which can validate the existence of Fe-V atomic pairs in FeV-NC [14,15].

X-ray diffraction (XRD) and X-ray photoelectron spectroscopy (XPS) were employed to analyze the detailed chemical composition of FeV-NC and reference materials. XRD measurements revealed a highly crystalline structure of the ZIF-8 skeleton that did not change when loaded with metal species (Fig. S5a). After pyrolysis at 900 °C, the typical peaks of ZIFs of all samples disappeared (Fig. S5b), leaving only broad bumps of the carbon substrate centered at 25° and 43°, indicating that Fe and V are uniformly distributed as atomic dispersions on the carbon substrate in the FeV-NC during the phase transition, which was aligned with HAADF-STEM, SAED and elemental mapping results. The surface chemical states of FeV-NC, Fe-NC and V-NC were further investigated by XPS (Fig. S6). The valence states of Fe and V in FeV-NC were evaluated and compared with those of reference materials (Fig. S7). Typical peaks of Fe and V metals were not observed in the XPS spectra of FeV-NC, Fe-NC and V-NC, demonstrating the absence of metal agglomerates, which is compatible with the results of the characterization by XRD and electron microscopy and further supports the atomic-level dispersion of Fe and V. The apparent binding energy shift in FeV-NC implies that the electronic structure of Fe has been altered due to the diatomic structure [10]. Graphite-N, pyridine-N and pyrrole-N can all be seen in the high-resolution N 1 s spectra of all materials (Fig. S8) [16]. In addition to these functional groups, the metal-nitrogen (M-N) bond at ~399.58 eV was generally observed in all M-NC samples, suggesting that the uncoordinated N group acts as an anchor point for the metal species, in agreement with previous reports [24–26]. The carbon base structure of the catalyst is demonstrated by the peak at 284.80 eV in the C 1s spectrum (Fig. S9), which is consistent with the findings of XRD and

SAED characterization. The conclusion drawn from the XPS pattern of N 1s is supported by the peak at 285.58 eV, which shows that there is a significant quantity of C-N structure. Throughout the XPS fine spectra of elemental N of the four materials, there is almost no peak shift, but the content of different types of N changes. Based on the integral area of the signal peaks of different types of N, their relative contents can be roughly estimated. Among them, the M-N in FeV-NC is significantly higher than that in the other three materials, which may be related to the introduction of more sites of metals. In addition, the highest content of graphitic N in NC may be due to the fact that less N is coordinated with metal atoms and more N is doped into graphite C. The C=O bonds on the carbon substrate are shown by the modest peak at 288.88 eV. These bonds were most likely formed at carbon flaws or material edges during high temperature pyrolysis. It is worth noting that little amount of Zn residues was also detected, resulting from incomplete volatilization during the pyrolysis of ZIF. As discussed below, such little amount of Zn will not notably contribute to electrocatalysis. [10,13]

X-ray absorption near-edge structure (XANES) and Fourier transformed (FT) extended X-ray absorption fine structure (EXAFS) measurements were performed to gather precise data on the electronic structures and coordination environment of the Fe and V atoms in FeV-NC. Fig. 3a depicts the Fe K-edge XANES spectra of FeV-NC, Fe foils, FeO and Fe<sub>2</sub>O<sub>3</sub> benchmarks, and the absorption edge of the Fe K-edge of FeV-NC is between FeO and Fe<sub>2</sub>O<sub>3</sub>, suggesting that the valence state of Fe is situated between +2 and +3. The results were consistent with the XPS results. A similar conclusion can be obtained from the XANES spectrum of V K-edge in Fig. 3b, in which the comparison with V foil and V oxides (V<sub>2</sub>O<sub>3</sub>, VO<sub>2</sub> and V<sub>2</sub>O<sub>5</sub>) shows that the valence state of V in FeV-NC is between 0 and +3. Fig. 3c and d show the FT of k<sup>3</sup>-weighted EXAFS oscillations in the R space for Fe and V in FeV-NC. The dominant peaks at 1.5 and 1.63 Å correspond to Fe-N and V-N/O first shell coordination, which is consistent with the observed metal-N bond in XPS [10–13]. An obvious peak at ~2.3 Å was observed in FeV-NC, corroborating the existence of Fe-V bond, which coincided with the peak at ~2.3 Å in the R-space of the V K edge (Fig. 3d) and proved the fact that Fe-V atom pairs exist in FeV-NC, in agreement with the ACHAADF-STEM and EELS results [10–13, 27–29]. The quantitative least-squares EXAFS curve-fitting analysis reveals the Fe-N<sub>4</sub> and O-V-N<sub>4</sub> coordination in FeV-NC (Fig. 3e, Fig. S10 and Table S2). According to the results of characterization and fitting, the FeV-NC model (Fig. 3f) was constructed for further DFT calculations. The same data processing method was used to analyze the XAS data of Fe-NC and V-NC, and the results are shown in Fig. S11. The Fe-V atom pair coordinated with one oxygen atom and six nitrogen atoms to form a diatomic site, and the Fe atom in Fe-NC coordinated with four nitrogen atoms to form a single atomic site. Similarly, the V atom in V-NC coordinates with one oxygen atom and four nitrogen atoms to form a single atomic site. Furthermore, EXAFS wavelet transform (WT) analysis was carried out to provide additional proof that the Fe-V connection existed (Fig. 3g–h). The diatomic Fe-V configuration should correspond to the newly emerging intensity maximum at ~2.3 Å in the spectrum of FeV-NC, which is not attributable to either the metallic Fe-Fe path or the V-V path and is extremely compatible with the characterization result of AC-HAADF-STEM [10].

### 3.2. Electrocatalytic performance of catalysts

Initially, the HER and OER activities of FeV-NC in 1 M KOH were investigated with a three-electrode system. The materials under study were loaded on nickel foams (NF) since NFs have the advantages of low cost, high electrical conductivity and three-dimensional skeleton. It has been previously reported that the contribution of NF to catalytic performance was negligible [5–8, 30, 31]. The linear sweep voltammetric (LSV) curves of HER show that FeV-NC is the best performing of all the materials tested, requiring only an overpotential of 88.8 mV as opposed to the Pt/C commercial catalyst with a 98.8 mV overpotential to drive a current density of 10 mA cm<sup>-2</sup> (Fig. 4a). It is also much less than the

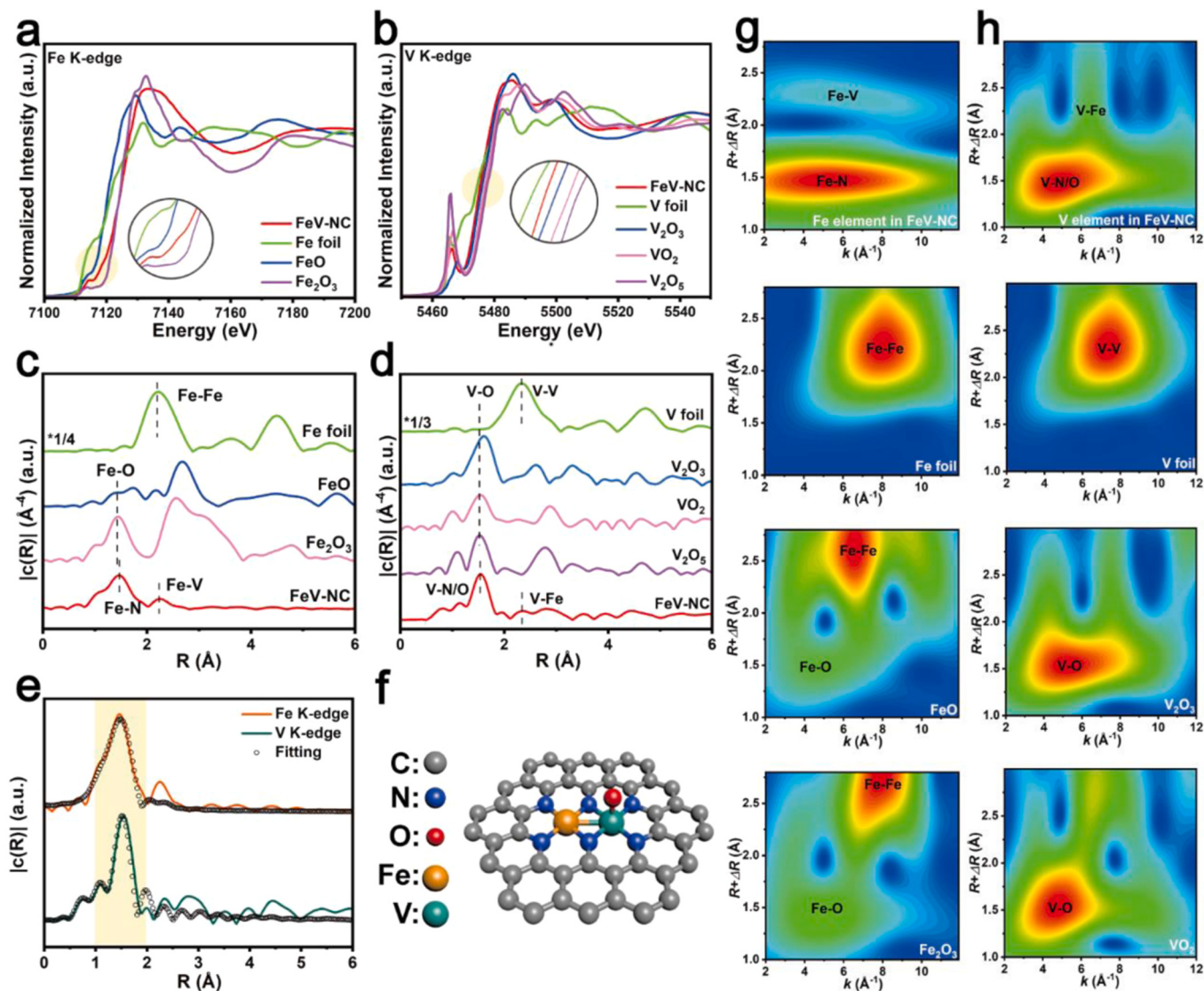


**Fig. 3.** Structural characterization of FeV-NC. (a) Fe K-edge XANES spectra and (b) V K-edge XANES spectra of FeV-NC and reference samples. (c) FT-EXAFS spectra at the Fe K-edge and (d) V K-edge of FeV-NC and reference samples. (e) Corresponding fitting in R space at the Fe K-edge and V K-edge of FeV-NC. (f) The optimized atomic structure of the Fe-V atom pair site. (g) WT of the Fe K-edge and (h) V K-edge for FeV-NC and reference samples.

159.8 mV of Fe-NC, 181.8 mV of V-NC, 192.8 mV of NC and 236.8 mV of NF [30,31]. According to Fig. 4b, the Tafel slope of HER polarization process of FeV-NC is 76.7 mV dec<sup>-1</sup>, which is much lower than that of Pt/C (80.8 mV dec<sup>-1</sup>), Fe-NC (98.1 mV dec<sup>-1</sup>), V-NC (101.1 mV dec<sup>-1</sup>), NC (113.0 mV dec<sup>-1</sup>) and NF (141.4 mV dec<sup>-1</sup>). Additionally, the intrinsic activity of the catalyst is an important indicator to evaluate the catalyst performance, which can be evaluated by calculating the conversion frequency (TOF) and mass activity (MA) at a certain overpotential (Fig. S12) [32]. At an overpotential of 140 mV, the TOF and MA values of FeV-NC were 0.92 s<sup>-1</sup> and 50.25 A g<sup>-1</sup>, respectively, which were better than those of Fe-NC (0.16 s<sup>-1</sup> and 6.76 A g<sup>-1</sup>) and V-NC (0.43 s<sup>-1</sup> and 5.10 A g<sup>-1</sup>). Besides, the electrochemical active area results showed that FeV-NC had a larger ECSA value which was evaluated by its C<sub>dl</sub> value, implying that the introduction of V increased the number of active sites or the degree of exposure (Fig. S13). Moreover, EIS test (Fig. S14) also showed that FeV-NC had the fastest electron transport speed in the process of HER [33]. Furthermore, the long-term stability test of HER at an overpotential of 89 mV showed that the current retention rate of FeV-NC was approximately 77.4 % for 20 h, while that of Pt/C was only 36.9 % for 20 h, implying that FeV-NC had stable HER catalytic performance (Fig. 4c). The excellent HER activity of

FeV-NC was also confirmed by comparison with the performance of previously reported catalysts (Fig. 4d) [31–44].

The LSV curves of OER are shown in Fig. 4e. In the control group, NF had the lowest catalytic activity and the overpotentials of Fe-NC and V-NC were 251.2 mV and 327.2 mV, respectively, 101 mV and 25 mV lower than those of NC, which proves that the metal single atom in the materials played a decisive role in the catalytic process. Even when compared to the commercial catalyst RuO<sub>2</sub>, the catalytic performance of Fe-NC is equivalent. However, after the introduction of V, FeV-NC shows more excellent OER performance than Fe-NC, suggesting that V increases the expressive capacity of the active site. When the current density reaches 10 mA cm<sup>-2</sup> and 50 mA cm<sup>-2</sup>, the required overpotentials are only 233.2 mV and 254.2 mV, respectively. It is noteworthy that RuO<sub>2</sub> also achieved a current density of 10 mA cm<sup>-2</sup> at an overpotential of 233.2 mV. However, at a current density of 50 mA cm<sup>-2</sup>, RuO<sub>2</sub> required 40 mV more overpotential than FeV-NC, demonstrating that despite its low overpotential, RuO<sub>2</sub> has slow kinetics as a commercial OER catalyst. In Fig. 4f, FeV-NC has the lowest Tafel slope (44.1 mV dec<sup>-1</sup>) compared with all controls, indicating that the reaction kinetics of FeV-NC are improved compared with those of Fe-NC, and also proving that the activity of the Fe-V dual-atom-site is much

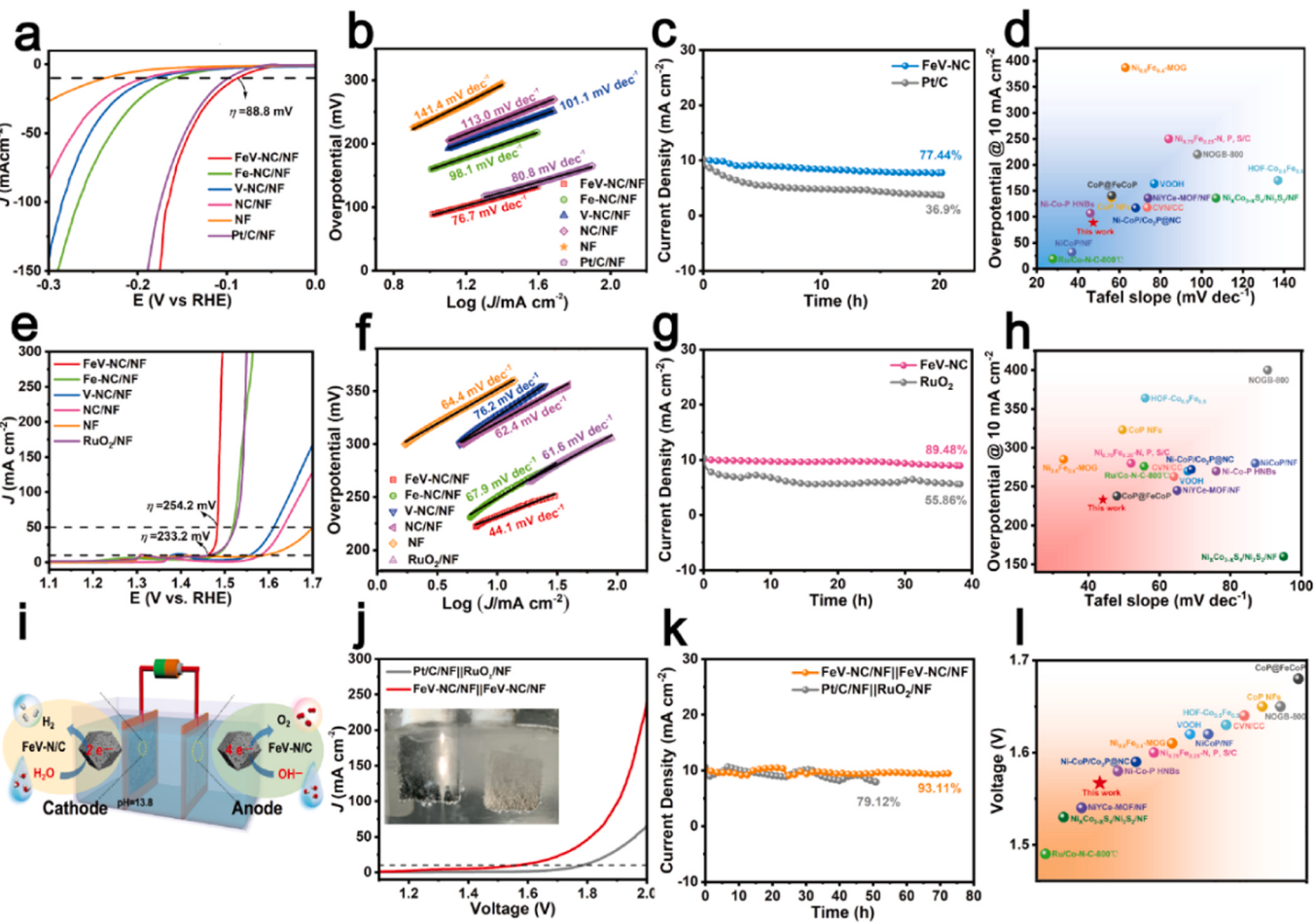


**Fig. 4.** Electrochemical catalytic performance assessment. (a) HER polarization curves and (b) corresponding Tafel plots of FeV-NC and reference samples. (c) Chronoamperometry test of FeV-NC for HER at a potential of  $-89$  mV. (d) Comparison of overpotential at  $10 \text{ mA cm}^{-2}$  and Tafel slope with previously reported HER catalysts. (e) OER polarization curves and (f) corresponding Tafel plots of FeV-NC and reference samples. (g) Chronoamperometry test of FeV-NC for OER at a potential of  $1.46$  V. (h) Comparison of overpotential at  $10 \text{ mA cm}^{-2}$  and Tafel slope with previously reported OER catalysts. (i) Schematic illustration of the experimental application for electrocatalytic OWS. (j) OWS polarization curves and (k) chronoamperometry curve of the electrolytic cell assembled by FeV-NC/NF||FeV-NC/NF at a potential of  $1.57$  V. (l) Comparison of potential at  $10 \text{ mA cm}^{-2}$  with previously reported OWS catalysts.

better than that of the Fe or V single-atom-site. The Tafel slope of RuO<sub>2</sub> is  $61.6 \text{ mV dec}^{-1}$ , proving that FeV-NC has markedly faster kinetics than RuO<sub>2</sub> [29,30]. Additionally, FeV-NC has a TOF value ( $0.5 \text{ s}^{-1}$ ) and MA value ( $54.5 \text{ A g}^{-1}$ ) that are substantially greater than those of Fe-NC ( $0.13 \text{ s}^{-1}$  and  $11.4 \text{ A g}^{-1}$ ) and V-NC ( $0.15 \text{ s}^{-1}$  and  $3.45 \text{ A g}^{-1}$ ) at an overpotential of  $254$  mV (Fig. S12). Moreover, the charge transport ability was evaluated by electrochemical impedance spectroscopy (EIS) at a potential of  $1.46$  V (vs. RHE) (Fig. S14). The results showed that FeV-NC had the lowest resistance, i.e., the fastest charge transport ability, which was consistent with the results of Tafel [33]. The long-term stability of the catalyst is also an important indicator to estimate the performance of the catalyst. The current retention rate of the catalyst was  $89.5\%$  after nearly  $40$  h of stability testing at an initial current density of  $10 \text{ mA cm}^{-2}$  at  $1.46$  V (vs. RHE) potential (Fig. 4g). The excellent OER catalytic performance of FeV-NC is further confirmed by comparing the overpotential of FeV-NC in this work with that of other previously reported catalysts at  $10 \text{ mA cm}^{-2}$  during OER (Fig. 4h), which shows that the OER catalytic performance of FeV-NC is comparable and even exceeds that of most of them [31–44].

Inspired by the excellent HER and OER bifunctional performance of FeV-NC, we further set up a two-electrode electrolyzer for OWS electrocatalysis using FeV-NC as both the anode and cathode (FeV-NC/NF||FeV-NC/NF) in  $1 \text{ M KOH}$  (Fig. 4i). As shown in Fig. 4j, the FeV-NC/NF||FeV-NC/NF electrolyzer requires only  $1.57$  V to drive a current density

of  $10 \text{ mA cm}^{-2}$ , while the RuO<sub>2</sub>/NF||Pt/C/NF electrolyzer requires  $1.78$  V, indicating that FeV-NC has superior electrocatalytic OWS performance compared to commercial catalysts. In addition, long-term stability test in Fig. 4k starting with  $10 \text{ mA cm}^{-2}$  showed that there was still a  $93.1\%$  current retention rate after  $75$  h, while the current retention rate of the RuO<sub>2</sub>/NF||Pt/C/NF electrolyzer after  $50$  h was only  $79.1\%$ , proving the good stability of FeV-NC/NF||FeV-NC/NF. In order to further demonstrate the good stability of the catalyst in terms of its structure and elemental state, SEM and XPS tests were conducted on the electrodes before and after the  $10$ -h long-term stability test under a current density of  $10 \text{ mA cm}^{-2}$  (Fig. S15). SEM images before and after the reactions showed that the morphology of the FeV-NC remained the same. XPS total spectrum showed no change in the kinds of elements. In addition, fine spectra represented by Fe and N elements showed almost no variations in the content and valence state of the elements before and after the reactions. The above experimental data show that FeV-NC has not only excellent catalytic activity but also good stability. The inset in Fig. 4j shows that the cathode and anode of FeV-NC/NF||FeV-NC/NF electrolyzer produce continuous H<sub>2</sub> and O<sub>2</sub> bubbles. In Fig. 4l, compared with the recently reported the bifunctional catalyst, FeV-NC shows better activity of OWS [31–44].

### 3.3. Exploration of catalytic mechanism

To better understand the mechanism of electrocatalytic reactions and the precise reactivity sites, HER and OER electrocatalytic processes on FeV-NC were examined utilizing in-situ electrochemical Raman methods. In term of HER, it was assumed that the metal Fe would be the active center. However, no interaction of Fe with H-/O-containing intermediates was observed in Fig. 5a in the range of 300–1100 cm<sup>-1</sup>. Unexpectedly, vibrational bands of the stretching modes of different N-H species (3293 and 3355 cm<sup>-1</sup>) were captured at -0.09 to -0.69 V (vs. RHE), in addition to the OCP potential [45]. From these implications, it is speculated that the N atoms coordinated to metals are most likely the active sites of HER. As shown in Fig. 5b, it is evident that no reaction processes occur at the open circuit potential (OCP), as demonstrated by the absence of substantial signals of important reaction intermediates in the range of 300–1100 cm<sup>-1</sup>, with the exception of the peak attributable to OH<sup>-</sup> at 991 cm<sup>-1</sup> [46]. Two peaks associated with the Fe<sup>III</sup>-O and Fe<sup>II</sup>-OH vibrations arise at 379 and 533 cm<sup>-1</sup>, respectively, when the potential hits 1.51 V (vs. RHE). As the potential continues to increase to 2.11 V (vs. RHE), the vibrational peak of Fe<sup>III</sup>-O diminishes, while at the same time, the peak intensity of Fe<sup>II</sup>-OH is enhanced, which is an indication of the transition from Fe<sup>III</sup>-O to Fe<sup>II</sup>-OH during the OER [47]. The vibrational bands corresponding to the reaction intermediates \*OOH, O-M-O, and \*OH (730, 802 and 1048 cm<sup>-1</sup>) are greatly strengthened, but the stretching vibrational band of the reactant OH<sup>-</sup> situated at 991 cm<sup>-1</sup> of OER is dramatically decreased at 0.5 and 1.1 V [48]. However, the peaks corresponding to \*OOH and O-M-O become weak at 1.1 V relative to 0.5 V, while the peaks corresponding to \*OH are enhanced, which may be due to the accelerated OER reaction rate and rapid O<sub>2</sub> desorption at high potentials, resulting in large reaction intermediate accumulation before the rate-determining step (RDS) and an obvious reaction intermediate consumption after the RDS [47,48]. This indicates that Fe is the main catalytically active center of OER, while the RDS is the conversion from the reaction intermediate \*OH to \*OOH. It should also be noted that the peak located near 450 cm<sup>-1</sup> is caused by the Raman scattering of the carbon atoms in the catalyst and not the reaction intermediate, so it is not labeled in the Fig. 5b.

Notably in Fig. 5b, the peak located at 1048 cm<sup>-1</sup> indicates the presence of preadsorbed \*OH on the catalyst surface, which may arise from the formation of coordination ligand between the metal in the catalyst and OH<sup>-</sup> in a strongly alkaline environment [49,50]. A series of studies have shown that the chemical environment of the active-sites in SACs, including ligand identity, coordination number and configuration, directly affects the electronic state, degree of freedom and other physicochemical properties of the active center related to reactant/intermediate adsorption, which in turn determines the catalytic performance of SACs [51–53]. The Gibbs free energy of the OER reaction before and after pre-adsorption of OH was calculated, compared and explored by DFT in the supporting information file (Fig. S16–19). But the reasons why dual-atom site catalysts (DASCs) outperform SACs remain open questions. Herein, the effects of neighboring V site have been investigated to gain a deeper understanding towards the origins of the improved performance of DASCs compared to SACs based on this scenario with pre-adsorbed \*OH. Therefore, it is important to note that the concept of pre-adsorbed \*OH serves as the foundation for all of the discussions that follow. According to the findings of XAS characterization, the V sites are saturated. Therefore, the \*OH observed by in situ Raman should be adsorbed on the unsaturated Fe sites. Accordingly, for the later DFT calculations, we have developed HO-FeN<sub>6</sub>V-O, HO-FeN<sub>4</sub> and VN<sub>4</sub>-O models (Fig. S16), respectively. As shown in Fig. S16a, the distance between Fe and V atoms in the HO-FeN<sub>6</sub>V-O model is 2.37 Å, which is highly consistent with the results characterized by XAS (~2.30 Å) and AC-HAADF-STEM (2.41 Å).

The Gibbs free energy of hydrogen adsorption is a vital descriptor for appraising HER activity, with a smaller |ΔG| value indicating stronger HER activity [12]. In view of the in situ Raman results of HER, the |ΔG|

of all N atoms in HO-FeN<sub>6</sub>V-O and HO-FeN<sub>4</sub> were first compared, and the results are shown in Fig. 5c, where the |ΔG| of two bridging N atom sites (N-a and N-b) are significantly lower than the other four coordination nitrogen atom sites (N-c, N-d, N-e, and N-f). In addition, the |ΔG| on the active sites of the HO-FeN<sub>4</sub> model were also calculated, as shown in Fig. S20, where the Fe site is superior to all coordinated nitrogen atoms, indicating that the active site of HER in HO-FeN<sub>4</sub> is Fe. Therefore, we inferred that this is the main reason for the HER enhancement of the diatomic catalyst, i.e., the neighboring V and Fe atoms create bridging N atoms and cause the reverse of HER activity from the Fe site in HO-FeN<sub>4</sub> to the bridging N site in HO-FeN<sub>6</sub>V-O. To verify this inference, the Gibbs free energies of the reaction paths on the Fe, V and N sites in HO-FeN<sub>6</sub>V-O, HO-FeN<sub>4</sub> and VN<sub>4</sub>-O was compared. As shown in Fig. 5d, among all the coordination N sites, the bridging N atom between Fe and V in HO-FeN<sub>6</sub>V-O presents a smaller |ΔG| (0.40 eV) than that of the Fe site in HO-FeN<sub>6</sub>V-O (0.58 eV), Fe site in HO-FeN<sub>4</sub> (0.62 eV) and V site in VN<sub>4</sub>-O (0.83 eV). Furthermore, we performed in-situ electrochemical Raman test on the HER process of Fe-NC. Compared with the test results of FeV-NC (Fig. S21a). There was no N-H signal in the test results of Fe-NC, but instead there were \*OH and O-Fe-O peaks, which proved that the active site of the HER process of Fe-NC is metal Fe (Fig. S21b), which was in agreement with the theoretical calculations, and indicated that after the introduction of V, the active site of the HER of Fe-NC was reversed from Fe to N.

In order to investigate the effects of the neighboring V atom on the active sites in the catalytic reaction path and to analyze the interactions, we performed calculations of projected density of state (PDOS) and electrochemical reaction path for three models, HO-FeN<sub>6</sub>V-O, HO-FeN<sub>4</sub> and VN<sub>4</sub>-O, and investigated their respective OER/HER mechanisms. The results of PDOS calculations (Fig. 5e) for the nitrogen atoms in HO-FeN<sub>6</sub>V-O indicate that the p<sub>z</sub> centers of the nitrogen atoms (N<sub>b</sub>) located at the bridging positions are closer to the Fermi energy level, which may be the origin of the HER activity of the bridging N atoms. The p<sub>z</sub> centers of these three kinds of nitrogen atoms are inversely related to the ΔG of the nitrogen atoms at the corresponding positions (Fig. 5f), indicating that the source of HER activity is closely related to the offset values of the p<sub>z</sub> centers of the nitrogen atoms [54], and it is also a consequence of the neighboring V site shifting the p<sub>z</sub> centers of the bridging nitrogen atoms in the positive direction. Therefore, the correlations between HER experimental performance and the calculated |ΔG| values unveil that the incorporation of neighboring V atom efficiently regulates the electron configuration of the bridging nitrogen atoms and the physicochemical interaction with the \*H intermediate, thus forming new HER active sites and promoting HER activity. This conclusion also confirmed our speculation that the active sites of HER were the coordination nitrogen atoms after we obtained the electrochemical in situ Raman spectra. Additionally, as water decomposition on the catalyst is a necessary step for HER in an alkaline environment, the excellent water absorption capacity is advantageous [33]. As shown in Fig. S22, the H<sub>2</sub>O adsorption energy on the Fe site in HO-FeN<sub>6</sub>V-O clearly decreases compared to that on the Fe site in HO-FeN<sub>4</sub> after the addition of VN<sub>4</sub>-O, which is consistent with the obtained values of |ΔG| and the results of electrolytic experiments [41]. The calculations and comparison results of Gibbs free energy and H<sub>2</sub>O adsorption energy are coordinated with the conclusions from PDOS as well as frontier orbitals, which not only confirm that the neighboring V atom has a tuning impact on HO-FeN<sub>4</sub> site, but also provide a theoretical foundation for the results of electrochemical experiments. To sum up from the theoretical investigation, the neighboring V atom boost HER via: 1) Forming a diatomic site with the Fe site and creating bridging N atoms as the new HER active sites; 2) shifting the p<sub>z</sub> centres of the bridging N atoms positively; 3) reducing the adsorption energy of the reaction substrate, i.e. H<sub>2</sub>O, on the catalyst surface.

In the term of OER, compared with HO-FeN<sub>4</sub> (Fig. 5g), the PDOS of d-band Fe in HO-FeN<sub>6</sub>V-O (Fig. 5h), at the Fermi level is significantly enhanced after the addition of VN<sub>4</sub>-O. Notably, d<sub>xy</sub><sup>2</sup> and d<sub>xy</sub> varies

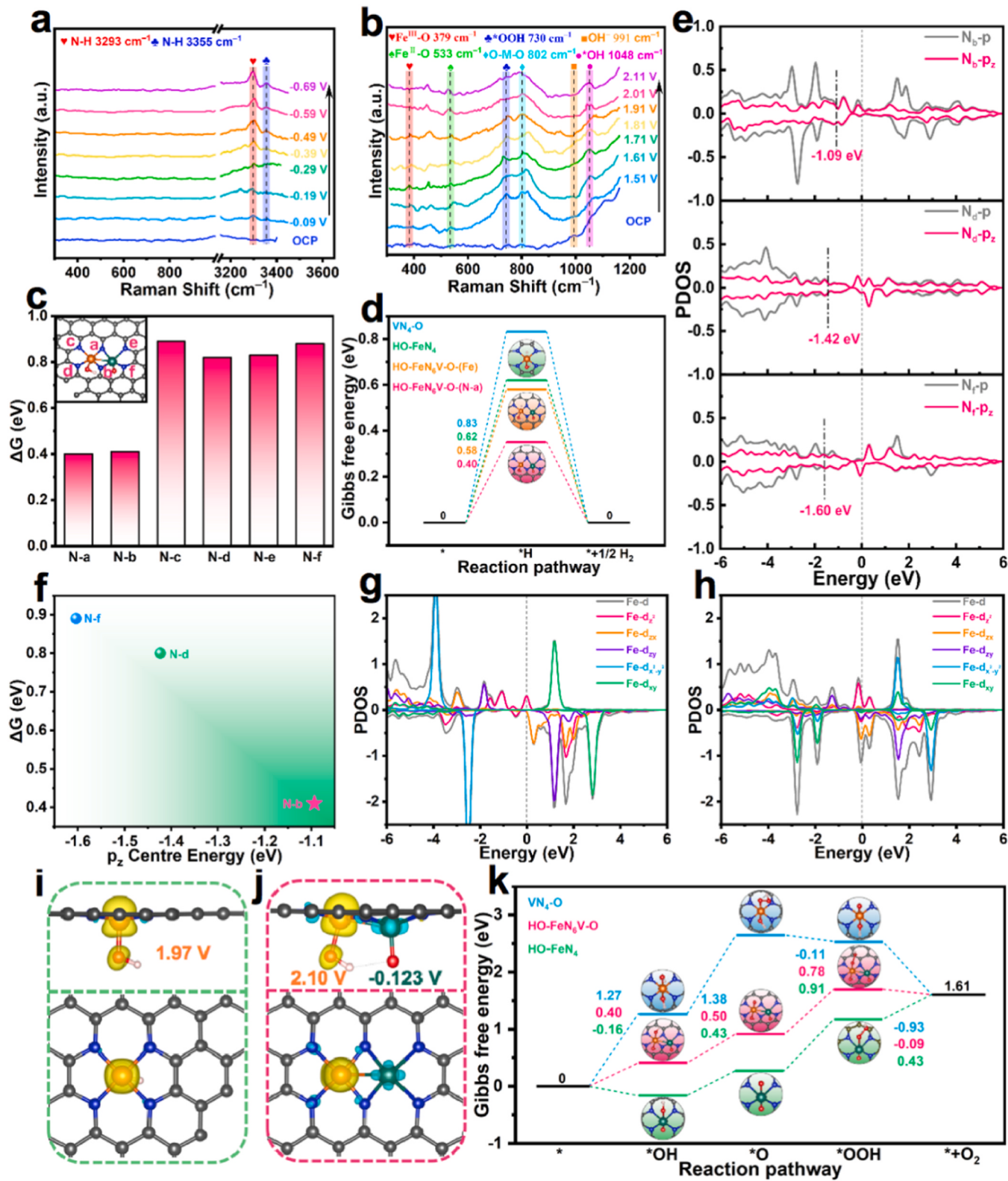


**Fig. 5.** In-situ Raman and DFT calculation results. Potential-dependent (vs. RHE) in situ Raman spectra during (a) HER and OER (b) processes of FeV-NC. (c) The coding of the coordination nitrogen atoms in HO-FeN<sub>6</sub>V-O and the corresponding Gibbs free energy difference for HER. (d) Gibbs free energy diagrams of HER process on VN<sub>4</sub>-O, HO-FeN<sub>4</sub>, the Fe site in the HO-FeN<sub>6</sub>V-O, and bridging N site in the HO-FeN<sub>6</sub>V-O. (e) Projected DOS on p bands and p<sub>z</sub> centre of N atoms in HO-FeN<sub>6</sub>V-O. (f) Relationship between the HER Gibbs free energy change and p<sub>z</sub>-center offset values corresponding to different positions of nitrogen atoms in HO-FeN<sub>6</sub>V-O. Projected DOS on d bands of Fe in (g) HO-FeN<sub>4</sub> and (h) HO-FeN<sub>6</sub>V-O. Magnetic moments of (i) HO-FeN<sub>4</sub> and (j) HO-FeN<sub>6</sub>V-O. (k) Gibbs free energy diagrams of OER process on VN<sub>4</sub>-O, HO-FeN<sub>6</sub>V-O, and HO-FeN<sub>4</sub> at pH=13.8, 0 V vs. RHE. The isosurface values of the spin electron densities are 0.01 e/Borh<sup>3</sup>.

significantly between HO-FeN<sub>6</sub>V-O and HO-FeN<sub>4</sub>, indicating the strong lateral d-d coupling on the x-y surface of Fe-V [26]. The electronic properties determined that constructing dual-atom-site centers via neighboring V atom could boost the reaction activity of the Fe site, which may modulate the interaction with OER/HER intermediates [33]. Meanwhile, the d-band of V is far away from the Fermi level, indicating that the adsorption exclusively occurs on the Fe site in HO-FeN<sub>6</sub>V-O (Fig. S23).

To further examine the changes in atomic orbital and electronic states induced by the d-d orbital coupling of Fe and V, the higher occupied molecular orbitals (HOMO) and spin densities of discrete HO-FeN<sub>4</sub> and VN<sub>4</sub>-O were exported and compared with their counterparts from HO-FeN<sub>6</sub>V-O. Apparently, the Fe sites in HO-FeN<sub>6</sub>V-O show more exposed d<sub>z</sub><sup>2</sup> and d<sub>zx</sub> characters in the spin-up and spin-down polarized HOMO states, respectively, with the contribution of VN<sub>4</sub>-O moiety compared to HO-FeN<sub>4</sub> sites, which is consistent with the results of PDOS. (Fig. S16) The introduction of V enhances the electronic spin of Fe, and the corresponding spin magnetic moment increases from 1.97 V to 2.10 V. Furthermore, after forming a diatomic site with Fe, the spin orientation of V shifts and is exactly opposite to the Fe atom, which may be more favorable to regulate the affinity of the active site for different reaction intermediates (Fig. 5i, j and S17) [55,56]. Compared with the calculations of other models, the VN<sub>4</sub>-O site has almost no contribution to HOMO, which would greatly limit its catalytic activity.

Similarly, OER Gibbs free-energy diagrams of the HO-FeN<sub>4</sub> and VN<sub>4</sub>-O single-atom sites as well as the HO-FeN<sub>6</sub>V-O diatomic sites were computed. OER is a four-step process consisting mainly of the adsorption and desorption of OH\*, O\*, and OOH\* intermediates (\* denotes an adsorption site) [57]. It is clear that the RDS for the Fe site in HO-FeN<sub>6</sub>V-O and HO-FeN<sub>4</sub> is the O\* + OH<sup>-</sup> → OOH\* + e<sup>-</sup> step, which is exactly consistent with the results of our in situ electrochemical Raman experiments (Fig. 5k), while for OER process on VN<sub>4</sub>-O, the RDS is the step from the intermediate OH\* to O\*. It should be noted that the Fe site in HO-FeN<sub>6</sub>V-O exhibits the lowest RDS energy barrier (0.78 eV) when compared to HO-FeN<sub>4</sub> (0.91 eV) and VN<sub>4</sub>-O (1.38 eV), indicating the lowest energy barrier for the OER process to occur at the HO-FeN<sub>6</sub>V-O. To sum up from the theoretical investigation, the neighboring V atom boost OER via: 1) increasing the exposure of the HOMO orbital of the Fe site but also introduced the opposite electron spin direction of the Fe atom; 2) forming a strong transverse d-d coupling on the x-y surface, and the d-band of Fe was simultaneously enhanced at the Fermi level in terms of the PDOS.

#### 4. Conclusion

In summary, we successfully reversed the HER activity from the metal Fe sites to the non-metal N sites by neighboring V atom, and simultaneously enhanced the OER activity at the Fe site, making it effective for electrocatalytic OWS. Potential-dependent in situ electrochemical Raman spectroscopy and DFT calculations indicate that the mechanism of neighboring V atom for the simultaneous reverse and enhancement on N and Fe sites: (i) the neighboring V atom indirectly creates specific bridging N atoms between Fe and V and offsets their p<sub>z</sub> centers, reversing bridging N atoms to act as HER active sites; (ii) under the strong lateral d-d coupling, the neighboring V atom increases the exposure of HOMO orbitals and electron spin of Fe atoms, which is conducive to the interaction between the catalyst and the intermediates. This work can deepen our understanding of bifunctional catalyst design and catalytic processes from the perspective of atomic-scale interatomic interactions and further guide the reasonable design of high-performance electrocatalytic OWS catalysts by engineering the interface environment approaching to the active sites.

#### CRediT authorship contribution statement

Xianbin Meng: Writing – review & editing, Writing – original draft,

Investigation, Formal analysis, Data curation, Conceptualization. Zhiqiang Zhao: Software, Formal analysis, Data curation, Conceptualization. Yuqing Lin: Writing – review & editing, Writing – original draft, Supervision, Resources, Project administration, Funding acquisition, Formal analysis, Conceptualization. Kai Li: Resources, Formal analysis. Youwen Liu: Writing – review & editing, Formal analysis. Wenming Sun: Writing – original draft, Software, Resources, Methodology, Formal analysis, Data curation. Tianyou Zhai: Writing – review & editing, Supervision, Resources, Formal analysis.

#### Declaration of Competing Interest

The authors declare that they have no known competing financial interests or personal relationships that could have appeared to influence the work reported in this paper.

#### Data availability

Data will be made available on request.

#### Acknowledgements

This work was financially supported by the National Natural Science Foundation, China (grant nos. 22074095 & 22374103 (Y.L.) and U21A2069 (T.Z.)) and Beijing Natural Science Foundation (grant nos. 2222005 (Y.L.)).

#### Author contributions

The project was conceptualized by Prof. Y. L. (Yuqing Lin), Prof. T. Z. and X. M. supervised this project. X. M. synthesized the catalysts, conducted the electrochemical tests, and the related data processing. Prof. Y. L. (Yuqing Lin), X. M., Z. Z. and Prof. W. S. performed and analyzed the DFT calculations. Prof. K. L. and Prof. Y. L. (Yuqing Lin) helped to analyze the characterization results. Z. Z. and X. M. performed the XAFS and the in situ Raman spectroscopy. Prof. Y. L. (Yuqing Lin) and X. M. wrote the original paper. Prof. T. Z., Prof. Y. L. (Yuqing Lin) and Prof. Y. L. (Youwen Liu) revised the paper. All authors discussed the results and assisted during manuscript preparation.

#### Appendix A. Supporting information

Supplementary data associated with this article can be found in the online version at doi:10.1016/j.apcatb.2024.123942.

#### References

- [1] J. Zhao, Y. Zhang, Y. Xia, B. Zhang, Y. Du, B. Song, H.-L. Wang, S. Li, P. Xu, Strong phosphide-metaphosphate interaction in RuP/CoNiP<sub>4</sub>O<sub>12</sub> for enhanced electrocatalytic water splitting, *Appl. Catal. B: Environ.* 328 (2023) 122447.
- [2] Z. He, Y. He, Y. Qiu, Q. Zhao, Z. Wang, X. Kang, L. Yu, L. Wu, Y. Jiang, Monolithic-structured nickel silicide electrocatalyst for bifunctionally efficient overall water splitting, *Appl. Catal. B: Environ.* 342 (2024) 123386.
- [3] K. Feng, R. Song, J. Xu, Y. Chen, C. Lu, Y. Li, W. Hofer, H. Lin, Z. Kang, J. Zhong, The S-Fe(Ni) sub-surface active sites for efficient and stable overall water splitting, *Appl. Catal. B: Environ.* 325 (2023) 122365.
- [4] X. Zhang, P. Zhai, Y. Zhang, Y. Wu, C. Wang, L. Ran, J. Gao, Z. Li, B. Zhang, Z. Fan, B. Zhang, Z. Fan, L. Sun, J. Hou, Engineering Single-Atomic Ni-N<sub>4</sub>-O sites on semiconductor photoanodes for high-performance photoelectrochemical water splitting, *J. Am. Chem. Soc.* 143 (2021) 20657–20669.
- [5] K. Dong, D.T. Tran, X. Li, S. Prabhakaran, D.H. Kim, N.H. Kim, J.H. Lee, Three-phase interface engineering via P-doped CoMo<sub>2</sub>S<sub>4</sub>-integrated Co<sub>4</sub>S<sub>3</sub>/Co<sub>2</sub>P enables high-efficiency overall water splitting, *Appl. Catal. B: Environ.* 344 (2024) 123649.
- [6] X. Zhang, A. Wu, D. Wang, Y. Jiao, H. Yan, C. Jin, Y. Xie, C. Tian, Fine-tune the electronic structure in Co-Mo based catalysts to give easily coupled HER and OER catalysts for effective water splitting, *Appl. Catal. B: Environ.* 328 (2023) 122474.
- [7] C. Hu, J. Hu, Z. Zhu, Y. Lu, S. Chu, T. Ma, Y. Zhang, H. Huang, Orthogonal charge transfer by precise positioning of silver single atoms and clusters on carbon nitride for efficient piezocatalytic pure water splitting, *Angew. Chem. Int. Ed.* 61 (2022) e202212397.

- [8] X. Lv, W. Wei, H. Wang, B. Huang, Y. Dai, Holey Graphitic Carbon Nitride (g-CN) Supported bifunctional single atom electrocatalysts for highly efficient overall water splitting, *Appl. Catal. B: Environ.* 264 (2020) 118521.
- [9] X. He, X. Han, X. Zhou, J. Chen, J. Wang, Y. Chen, L. Yu, N. Zhang, J. Li, S. Wang, H. Jin, Electronic modulation with Pt-incorporated NiFe layered double hydroxide for ultrastable overall water splitting at 1000 mA cm<sup>-2</sup>, *Appl. Catal. B: Environ.* 331 (2023) 122683.
- [10] M. Xiao, J. Zhu, S. Li, G. Li, W. Liu, Y.-P. Deng, Z. Bai, L. Ma, M. Feng, T. Wu, D. Su, J. Lu, A. Yu, Z. Chen, 3d-orbital occupancy regulated Ir-Co atomic pair toward superior bifunctional oxygen electrocatalysis, *ACS Catal.* 11 (2021) 8837–8846.
- [11] C. Rong, X. Shen, Y. Wang, L. Thomsen, T. Zhao, Y. Li, X. Lu, R. Amal, C. Zhao, Electronic structure engineering of single-atom Ru sites via Co-N<sub>4</sub> sites for bifunctional ph-universal water splitting, *Adv. Mater.* 34 (2022) e2110103.
- [12] J. Xu, S. Lai, D. Qi, M. Hu, X. Peng, Y. Liu, W. Liu, G. Hu, H. Xu, F. Li, C. Li, J. He, L. Zhuo, J. Sun, Y. Qiu, S. Zhang, J. Luo, X. Liu, Atomic Fe-Zn dual-metal sites for high-efficiency ph-universal oxygen reduction catalysis, *Nano Res.* 14 (2020) 1374–1381.
- [13] Z. Yu, C. Si, A.P. LaGrow, Z. Tai, W.A. Caliebe, A. Tayal, M.J. Sampaio, J.P. S. Sousa, I. Amorim, A. Araujo, L. Meng, J.L. Faria, J. Xu, B. Li, L. Liu, Iridium–iron diatomic active sites for efficient bifunctional oxygen electrocatalysis, *ACS Catal.* 12 (2022) 9397–9409.
- [14] D.S. Su, M. Havecker, W.M. illinger, R. Schlogl, Chemical and electron beam reduction of vanadium oxides monitored by EELS and NEXAFS, *Microsc. Microanal.* 7 (2020) 440–441.
- [15] A. Gloter, J. Ingrin, D. Bouchet, C. Colliex, Composition and Orientation Dependence of the O K and Fe L<sub>2,3</sub> EELS fine structures in Ca<sub>2</sub>(Al<sub>x</sub>Fe<sub>1-x</sub>)<sub>2</sub>O<sub>5</sub>, *Phys. Rev. B* 61 (2000) 2587–2594.
- [16] K. Artyushkova, B. Kiefer, B. Halevi, A. Knop-Gericke, R. Schlogl, P. Atanassov, Density functional theory calculations of XPS binding energy shift for nitrogen-containing graphene-like structures, *Chem. Commun.* 49 (2013) 2539–2541.
- [17] C. Feng, M.B. Faheem, J. Fu, Y. Xiao, C. Li, Y. Li, Fe-based electrocatalysts for oxygen evolution reaction: progress and perspectives, *ACS Catal.* 10 (2020) 4019–4047.
- [18] W. Wan, Y. Zhao, S. Wei, C.A. Triana, J. Li, A. Arcifa, C.S. Allen, R. Cao, G. R. Patzke, Mechanistic insight into the active centers of single/dual-atom Ni/Fe-based oxygen electrocatalysts, *Nat. Commun.* 12 (2021) 5589.
- [19] Z. Zhang, J. Hao, Y. Lu, Y. Xu, L. Li, W. Shi, Ink-assisted synthetic strategy for stable and advanced composite electrocatalysts with single Fe sites, *Small* 16 (2020) e2006113.
- [20] J. Wang, H. Li, S. Liu, Y. Hu, J. Zhang, M. Xia, Y. Hou, J. Tse, J. Zhang, Y. Zhao, Turning on Zn 4s electrons in a N<sub>2</sub>-Zn-B<sub>2</sub> configuration to stimulate remarkable ORR performance, *Angew. Chem. Int. Ed.* 60 (2021) 181.
- [21] J. Zhang, M. Zhang, Y. Zeng, J. Chen, L. Qiu, H. Zhou, C. Sun, Y. Yu, C. Zhu, Z. Zhu, Single Fe atom on hierarchically porous S, N-codoped nanocarbon derived from porphyrin enable boosted oxygen catalysis for rechargeable Zn-air batteries, *Small* 15 (2019) 1900307.
- [22] K. Yuan, D.F. Lützenkirchen-Hecht, L. Li, L. Shuai, Y. Li, R. Cao, M. Qiu, X. Zhuang, Y. Chen, M.K.H. Leung, U. Scherf, Boosting oxygen reduction of single iron active sites via geometric and electronic engineering: nitrogen and phosphorus dual-coordination, *J. Am. Chem. Soc.* 142 (2020) 2404.
- [23] G.-L. Hou, T. Yang, M. Li, J. Vanbuel, O.V. Lushchikova, P. Ferrari, J.M. Bakker, E. Janssens, Water splitting by C60-supported vanadium single atoms, *Angew. Chem. Int. Ed.* 60 (2021) 27095.
- [24] Y. Wang, Z. Li, P. Zhang, Y. Pan, Y. Zhang, Q. Cai, S.R.P. Silva, J. Liu, G. Zhang, X. Sun, Z. Yan, Flexible carbon nanofiber film with diatomic Fe-Co sites for efficient oxygen reduction and evolution reactions in wearable zinc-air batteries, *Nano Energy* 87 (2021) 106147.
- [25] W. Ren, X. Tan, W. Yang, C. Jia, S. Xu, K. Wang, S.C. Smith, C. Zhao, Isolated diatomic Ni-Fe metal-nitrogen sites for synergistic electroreduction of CO<sub>2</sub>, *Angew. Chem. Int. Ed.* 58 (2019) 6972–6976.
- [26] Z. Zeng, L.Y. Gan, H.B. Yang, X. Su, J. Gao, W. Liu, H. Matsumoto, J. Gong, J. Zhang, W. Cai, Z. Zhang, Y. Yan, B. Liu, P. Chen, Orbital coupling of heterodiatomic nickel-iron site for bifunctional electrocatalysis of CO<sub>2</sub> reduction and oxygen evolution, *Nat. Commun.* 12 (2021) 4088.
- [27] Y. Wu, C. Ye, L. Yu, Y. Liu, J. Huang, J. Bi, L. Xue, J. Sun, J. Yang, W. Zhang, X. Wang, P. Xiong, J. Zhu, Soft template-directed interlayer confinement synthesis of a Fe-Co dual-single-atom catalyst for Zn-air batteries, *Energy Storage Mater.* 45 (2022) 805–813.
- [28] C. Liu, T. Li, X. Dai, J. Zhao, D. He, G. Li, B. Wang, X. Cui, Catalytic activity enhancement on alcohol dehydrogenation via directing reaction pathways from single- to double-atom catalysis, *J. Am. Chem. Soc.* 144 (2022) 4913–4924.
- [29] Y. Wang, X. Wan, J. Liu, W. Li, Y. Li, X. Guo, X. Liu, J. Shang, J. Shui, Catalysis stability enhancement of Fe/Co dual-atom site via phosphorus coordination for proton exchange membrane fuel cell, *Nano Res.* 15 (2022) 3082–3089.
- [30] Y. Zhou, G. Chen, Q. Wang, D. Wang, X. Tao, T. Zhang, X. Feng, K. Müllen, Fe-N-C electrocatalysts with densely accessible Fe-N<sub>4</sub> sites for efficient oxygen reduction reaction, *Adv. Funct. Mater.* 31 (2021) 2102420.
- [31] J. Wang, Y. Gao, T.L. You, F. Ciucci, Bimetal-decorated nanocarbon as a superior electrocatalyst for overall water splitting, *J. Power Sources* 401 (2018) 312–321.
- [32] M. Xiao, Z. Xing, Z. Jin, C. Liu, J. Ge, J. Zhu, Y. Wang, X. Zhao, Z. Chen, Preferentially engineering FeN<sub>4</sub> edge sites onto graphitic nanosheets for highly active and durable oxygen electrocatalysis in rechargeable Zn-air batteries, *Adv. Mater.* 32 (2020) e2004900.
- [33] H. Shi, H. Liang, F. Ming, Z. Wang, Efficient overall water-splitting electrocatalysis using lepidocrocite VOOH hollow nanospheres, *Angew. Chem. Int. Ed.* 56 (2017) 573–577.
- [34] F. Li, M. Jiang, C. Lai, H. Xu, K. Zhang, Z. Jin, Yttrium- and cerium-codoped ultrathin metal-organic framework nanosheet arrays for high-efficiency electrocatalytic overall water splitting, *Nano Lett.* 22 (2022) 7238–7245.
- [35] J. Shi, F. Qiu, W. Yuan, M. Guo, Z.-H. Lu, Nitrogen-doped carbon-decorated yolk-shell Cop@fecop micro-polyhedra derived from MOF for efficient overall water splitting, *Chem. Eng. J.* 403 (2021) 126312.
- [36] L. Ji, J. Wang, X. Teng, T.J. Meyer, Z. Chen, CoP nanoframes as bifunctional electrocatalysts for efficient overall water splitting, *ACS Catal.* 10 (2019) 412–419.
- [37] R. Bose, R.V. Jothi, K. Karuppasamy, A. Alfantazi, S.C. Yi, High performance multicomponent bifunctional catalysts for overall water splitting, *J. Mater. Chem. A* 8 (2020) 13795–13805.
- [38] E. Hu, Y. Feng, J. Nai, D. Zhao, Y. Hu, X.W. Lou, Construction of hierarchical Ni-CoP hollow nanobricks with oriented nanosheets for efficient overall water splitting, *Energ. Environ. Sci.* 11 (2018) 872–880.
- [39] Q. Hu, G. Li, R. Liu, B. Zhu, X. Chai, Q. Zhang, J. Liu, C. He, Trifunctional electrocatalysis on dual-doped graphene nanorings-integrated boxes for efficient water splitting and Zn-air batteries, *Adv. Energy Mater.* 9 (2019) 1803867.
- [40] H. Liang, A.N. Gandi, D.H. Anjum, X. Wang, U. Schwingenschlögl, H.N. Alshareef, Plasma-assisted synthesis of NiCoP for efficient overall water splitting, *Nano Lett.* 16 (2016) 7718–7725.
- [41] X. Zhang, H. Zhao, C. Li, S. Li, K. Liu, L. Wang, Facile coordination driven synthesis of metal-organic gels toward efficiently electrocatalytic overall water splitting, *Appl. Catal. B: Environ.* 299 (2021) 120641.
- [42] F.Q. Liu, J.W. Liu, Z. Gao, L. Wang, X.-Z. Fu, L.X. Yang, Y. Tao, W.H. Yin, F. Luo, Constructing Bimetal-complex based hydrogen-bonded framework for highly efficient electrocatalytic water splitting, *Appl. Catal. B: Environ.* 258 (2019) 117973.
- [43] H. Chu, P. Feng, B. Jin, G. Ye, S. Cui, M. Zhang, G.-X. Zhang, M. Yang, In-situ release of phosphorus combined with rapid surface reconstruction for Co-Ni bimetallic phosphides boosting efficient overall water splitting, *Chem. Eng. J.* 433 (2022) 133523.
- [44] S. Dutta, A. Indra, Y. Feng, H. Han, T. Song, Promoting electrocatalytic overall water splitting with nanohybrid of transition metal nitride-oxynitride, *Appl. Catal. B: Environ.* 241 (2019) 521–527.
- [45] Y. Zhao, F. Li, W. Li, Y. Li, C. Liu, Z. Zhao, Y. Shan, Y. Ji, L. Sun, Identification of M-NH<sub>2</sub>-NH<sub>2</sub> intermediate and rate determining step for nitrogen reduction with bioinspired sulfur-bonded FeW catalyst, *Angew. Chem. Int. Ed.* 60 (2021) 20331–20341.
- [46] F. Kong, M. Wang, Y. Huang, G. Meng, M. Chen, H. Tian, Y. Chen, C. Chen, Z. Chang, X. Cui, J. Shi, Cu-N-bridged Fe-3d Electron state regulations for boosted oxygen reduction in flexible battery and PEMFC, *Energy Storage Mater.* 54 (2023) 533–542.
- [47] M. Jian, C. Fu, R. Cheng, W. Zhang, T. Liu, R. Wang, J. Zhang, B. Sun, Integrated and binder-free air cathodes of Co<sub>3</sub>Fe<sub>7</sub> nanoalloy and Co<sub>5.47</sub>N encapsulated in nitrogen-doped carbon foam with superior oxygen reduction activity in flexible aluminum-air batteries, *Adv. Sci.* 7 (2020), 2000747.
- [48] M. Jiang, F. Wang, F. Yang, H. He, J. Yang, W. Zhang, J. Luo, J. Zhang, C. Fu, Rationalization on high-loading iron and cobalt dual metal single atoms and mechanistic insight into the oxygen reduction reaction, *Nano Energy* 93 (2022) 106793.
- [49] Y. Yang, H. Zhang, Z. Liang, Y. Yin, B. Mei, F. Song, F. Sun, S. Gu, Z. Jiang, Y. Wu, Z. Zhu, Role of local coordination in bimetallic sites for oxygen reduction: a theoretical analysis, *J. Energy Chem.* 44 (2020) 131–137.
- [50] P. Zhu, X. Xiong, X. Wang, C. Ye, J. Li, W. Sun, X. Sun, J. Jiang, Z. Zhuang, D. Wang, Y. Li, Regulating the FeN<sub>4</sub> moiety by constructing Fe-Mo dual-metal atom sites for efficient electrochemical oxygen reduction, *Nano Lett.* 22 (2022) 9507–9515.
- [51] J. Jin, X. Han, Y. Fang, Z. Zhang, Y. Li, T. Zhang, A. Han, J. Liu, Microenvironment engineering of Ru single-atom catalysts by regulating the cation vacancies in NiFe-layered double hydroxides, *Adv. Funct. Mater.* 32 (2022) 2109218.
- [52] Y. Ren, Y. Tang, L. Zhang, Z. Liu, L. Li, S. Miao, D.S. Su, A. Wang, J. Li, T. Zhang, Unraveling the coordination structure-performance relationship in Pt1/Fe<sub>2</sub>O<sub>3</sub> single-atom catalyst, *Nat. Commun.* 10 (2019) 4500.
- [53] Y. Wang, G. Jia, X. Cui, X. Zhao, Q. Zhang, L. Gu, L. Zheng, L.H. Li, Q. Wu, D. J. Singh, D. Matsumura, T. Tsuji, Y.-T. Cui, J. Zhao, W. Zheng, Coordination number regulation of molybdenum single-atom nanozyme peroxidase-like specificity, *Chem* 7 (2021) 436–449.
- [54] S.F. Yulk, V.R. Cooper, Tuning oxygen electrocatalysis via strain on LaNiO<sub>3</sub>(001), *Phys. Chem. Chem. Phys.* 21 (2019) 4738–4745.
- [55] W. Zhong, Y. Qiu, H. Shen, X. Wang, J. Yuan, C. Jia, S. Bi, J. Jiang, Electronic spin moment as a catalytic descriptor for Fe single-atom catalysts supported on C<sub>2</sub>N, *J. Am. Chem. Soc.* 143 (2021) 4405–4413.
- [56] Y.-N. Gong, W. Zhong, Y. Li, Y. Qiu, L. Zheng, J. Jiang, H.-L. Jiang, Regulating photocatalysis by spin-state manipulation of cobalt in covalent organic frameworks, *J. Am. Chem. Soc.* 142 (2020) 16723–16731.
- [57] G. Chen, P. Liu, Z. Liao, F. Sun, Y. He, H. Zhong, T. Zhang, E. Zschech, M. Chen, G. Wu, J. Zhang, X. Feng, Zinc-mediated template synthesis of Fe-N-C electrocatalysts with densely accessible Fe-N<sub>x</sub> active sites for efficient oxygen reduction, *Adv. Mater.* 32 (2020) e1907399.